Template-Free Synthesis of Nanoporous Nickel and Alloys as Binder- Free Current Collectors of Li Ion Batteries

Lu, Liqiang; Andela, Paul; De Hosson, J.T.M.; Pei, Yutao T.

Published in:
ACS Applied Nano Materials

DOI:
10.1021/acsanm.8b00284

Publication date:
2018

ACS APPLIED NANO MATERIALS

Article

Cite This: ACS Appl. Nano Mater. 2018, 1, 2206−2218

www.acsanm.org

Template-Free Synthesis of Nanoporous Nickel and Alloys as Binder-Free Current Collectors of Li Ion Batteries

Liqiang Lu,[†] Paul Andela,[†] Jeff Th.M. De Hosson,[‡] and Yutao Pei*[,†]

[†]Advanced Production Engineering, Engineering and Technology Institute Groningen, Faculty of Science and Engineering, University of Groningen, Nijenborgh 4, 9747 AG Groningen, The Netherlands

[‡]Department of Applied Physics, Zernike Institute for Advanced Materials, Faculty of Science and Engineering, University of Groningen, Nijenborgh 4, 9747 AG Groningen, The Netherlands

Supporting Information

ABSTRACT: This paper reports a versatile template-free method based on the hydrogen reduction of metallic salts for the synthesis of nanoporous Ni and alloys. The approach involves thermal decomposition and reduction of metallic precursors followed with metal cluster nucleation and ligament growth. Topological disordered porous architectures of metals with a controllable distribution of pore size and ligament size ranging from tens of nanometers to micrometers are synthesized. The reduction processes are scrutinized through X-ray diffraction, scanning electron microscopy, and transmission electron microscopy. The formation mechanism of the nanoporous metal is qualitatively explained. The as-prepared nanoporous Ni was tested as binder-free current collectors for nickel oxalate anodes of lithium ion batteries. The nanoporous Ni electrodes deliver enhanced reversible capacities and cyclic performances compared with commercial Ni foam. It is confirmed that this synthesis method has versatility not only because it is suitable for different types of metallic salts precursors but also for various other metals and alloys.

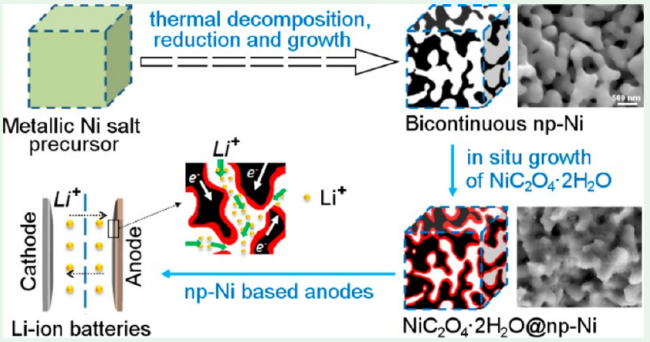

KEYWORDS: *nanoporous metals, Ni, alloys, current collectors, anode, electrochemical performance, lithium ion batteries*

1. INTRODUCTION

Three-dimensional (3D) nanoporous metallic structures have shown potential applications in electrochemically or chemically driven actuators, batteries, and supercapacitors, hydrogen or carbon dioxide reduction, catalyst, templates, and heat exchangers.[1−11] Applications can also be anticipated as reinforcement skeletons across composite materials, bioengineering implants, drug-delivery platforms, and as selective nanofilters for liquid purification.[13−16] In comparison with porous ceramics, they may exhibit higher electric conductivity and mechanical stability. The increasing requirements of low density and high stiffness materials in the automotive, biomedical, and aerospace industries also stimulated the search for specific nanoporous material systems.

For sustainable energy and controlling carbon dioxide emission, 3D porous metals (e.g., porous Ni and copper) particularly accelerate the fast development of electrochemical energy storage devices such as Li ion batteries and supercapacitors in recent years. Excellent performances such as high capacity, rate performances, and long-term cycling have been achieved by using nanoporous metals, attributed to their good conductivity, mechanical properties, and interconnected porous channels for ions diffusion.[1,3,5,6] For instance, the nanocrystalline MnO_2 loaded on nanoporous gold current collectors presented a specific capacitance of ∼1145 F/g.[3] 3D porous metal electrodes assisted the C-rates to approach 400 and 1000 C (the C-rate is the time in hours required to fully charge or discharge an electrode or battery; an *n* C-rate indicates that the current chosen will discharge the system in 1/*n* h) for lithium ion and nickel−metal hydride chemistries, which means the battery can finish the discharge and charge within minutes. In contrast to the commercial nickel foams, nanoporous metallic structures can largely increase the loading of active materials, surface area, and contact between active materials and ligaments.[1,3,5,6] The bifunction of nanoporous metals as both current collector and host for active materials could significantly improve the gravimetric and volumetric capacity of electrodes because of their lightweight and abandoning binders and electric conductive additives. Although many efforts have been made for developing nanoporous metallic current collectors for energy storage, their applications are still hampered by many issues including high cost of gold-based electrodes, low loading of active materials, low areal, gravimetric, and volumetric capacities of electrodes due to the use of supporting materials, and low loading of active materials, nonuniform deposition of

Received: February 20, 2018
Accepted: April 19, 2018
Published: April 19, 2018

active materials, as well as the problems in the synthesis of nanoporous metals.

The current most popular method for synthesizing nanoporous metals is selective leaching or dealloying.[1,12,13,17,18] The starting materials are binary solid solutions. During etching, the less noble constituent is selectively dissolved; meanwhile, the nobler part remains and simultaneously rearranges to form the bicontinuous porous microstructure with interpenetrating pores and solid phase. However, there are many issues with the dealloying method. First, specially prepared binary or ternary alloys with alloying elements in solid solution are required. Second, the etching time may become rather extensive particularly for bulk alloys due to the resistance of ions volumetric diffusion. So it is hard to synthesize large-size nanoporous metals by dealloying. Also, the etching process may introduce impurities from etchants and oxides into the porous structure.[4] Another approach for preparation of nanoporous systems is by sintering of nanoparticles or nanosized powder, which is a process of aggregation and coalescence of metal nanoparticles.[1,19] But normally the preparation of the metallic nanoparticles is another difficult issue. A third commonly known method is by sacrificing templates, in which metallic precursors are first filled by electroplating or infiltration casting, followed with removal of the templates by firing or chemical etching. These templates can be self-assembly copolymers, polyurethane foam, silica (SiO_2) foam, plastic particles, etc.,[1,4,6,13,18] but their synthesis, filling metals into and removal of the templates are rather complicated. In the assistance of electrolytically generated hydrogen bubbles that serve as pore-forming agent, porous metals or alloys have been also achieved during electrodeposition.[20] But this method is still limited to producing porous films and rather difficult for making bulk porous metals.[20,21] The self-assembly technique has advantages in nanoporous metal nanocrystals but limitations in bulks.[22] The combustion synthesis and pyrolysis of metal salt/dextran normally require multiple processes, complexes, and organics to produce the precursor and also easily introduce impurities such as carbon and nitrogen.[1,13] Recently, Kreder III et al. reported synthesis of porous metals by microwave solvothermal method in solution,[23] but control still requires considerable efforts. The search for a facile and inexpensive method for large-scale production of nanoporous metals is still a challenge. This is particularly true for the field of electrochemical energy storage devices such as lithium ion batteries and supercapacitors.[24,25]

Motivated by these requests for mass production of nanoporous metals and alloys, we developed a facile, fast, and template-free method, which is the hydrogen reduction of relevant metallic salts and consequent growth of porous structures. The as-reported method only requires metallic salts that contain the desired metal elements and hydrogen as a reducing gas, instead of using any hard or soft templates, complexes, and binary/ternary alloys. The formation of 3D bicontinuous nanoporous structure involves the thermal decomposition and hydrogen reduction of metal salts and a subsequent rearrangement and growth of reduced metallic species.

In the following we show that it is possible to synthesize topological nanoporous Ni over a very wide range of pore sizes, that is, from tens of nanometers to micrometers. In addition nanoporous cobalt and Ni−Co alloy are also made to demonstrate the versatility of the method. For potential application, the nanoporous metals are also used as binder-free current collectors for lithium ion batteries. The as-prepared electrodes exhibit high reversible capacity, good cyclic performances and rate performances ascribed to the good conductivity, and topological nanoporous architectures.

2. EXPERIMENTAL SECTION

Scheme 1 illustrates the overall process from the synthesis of nanoporous Ni (or alloys) to the application of nanoporous Ni as

Scheme 1[a]

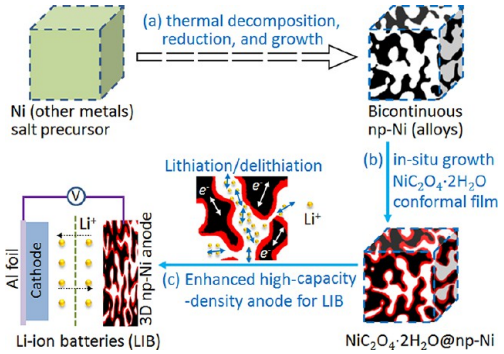

[a]Schematic illustration of synthesis of nanoporous Ni and alloys by the thermal decomposition, reduction, and metallic growth, in-situ growth of $NiC_2O_4{\cdot}H_2O$ coated np-Ni, and the use of lightweight nanoporous Ni as binder-free current collectors for Li ion batteries.

current collectors for Li ion batteries. Step (a) shows the thermal decomposition of metallic salt precursor, reduction, and metallic growth of nanoporous metals. The size of ligaments and pores can be controlled by the temperature and growth time according to the formation mechanism and growth kinetics of nanoporous metals. Step (b) is the in situ growth of $NiC_2O_4{\cdot}2H_2O$ active materials on the ligaments of np-Ni. The microstructures and loading of $NiC_2O_4{\cdot}2H_2O$ can be controlled. A conformal coating is preferred due to the good intimate contact between active materials and Ni ligaments. For the electrochemical application shown in Step (c), owing to the lightweight and binder-free benefits, the as-synthesized $NiC_2O_4{\cdot}2H_2O$@np-Ni electrodes exhibit high areal capacity and capacity densities.

2.1. Preparation of Nanoporous Metals (np-Me). Preparation of nanoporous nickel (np-Ni): Typically, 29 g of nickel nitrate hexahydrate was preheated in air or argon at 100−200 °C until it became solid, and then it was heated to a temperature of 250−800 °C at a heating rate of 5 °C/min for hydrogen reduction. During reduction, 100 sccm of H_2/Ar (5−15 vol % H_2) was introduced. The sample was held at the selected temperature for 2 h. After it cooled, nanoporous Ni was collected. For the other nickel salts precursors, the procedures were kept the same as used for nickel nitrate hexahydrate.

Preparation of np-Co: The np-Co was synthesized by using the same processes for pure Ni, except that cobalt nitrate hexahydrate was taken as the precursor.

Preparation of np-NiCo alloy: The np-NiCo alloy was also synthesized by using the same processes for pure Ni, except for using the mixture of cobalt nitrate hexahydrate and nickel(II) nitrate hexahydrate. Before they were preheated, 36.6 g of cobalt nitrate hexahydrate and 29 g of nickel(II) nitrate hexahydrate were mixed in water, and the mixture was collected after evaporation of water by stirring at 50 °C.

Preparation of $NiC_2O_4{\cdot}2H_2O$@np-Ni: Ni precursors were pressed into chips with size ø15 mm × 400 μm. The np-Ni chips were produced by reduction of Ni precursors at 600 °C for 2 h. The as-prepared Ni chips polished from one side to ∼100 μm. For synthesis of $NiC_2O_4{\cdot}2H_2O$@np-Ni, the as-prepared np-Ni chips were put in 0.3 M solution of oxalic acid dihydrate in water and kept reacting at 45 °C for 1.5 h. Subsequently, the $NiC_2O_4{\cdot}2H_2O$@np-Ni chips were washed with ethanol and dried for 2 h at 60 °C.

DOI: 10.1021/acsanm.8b00284
ACS Appl. Nano Mater. 2018, 1, 2206−2218

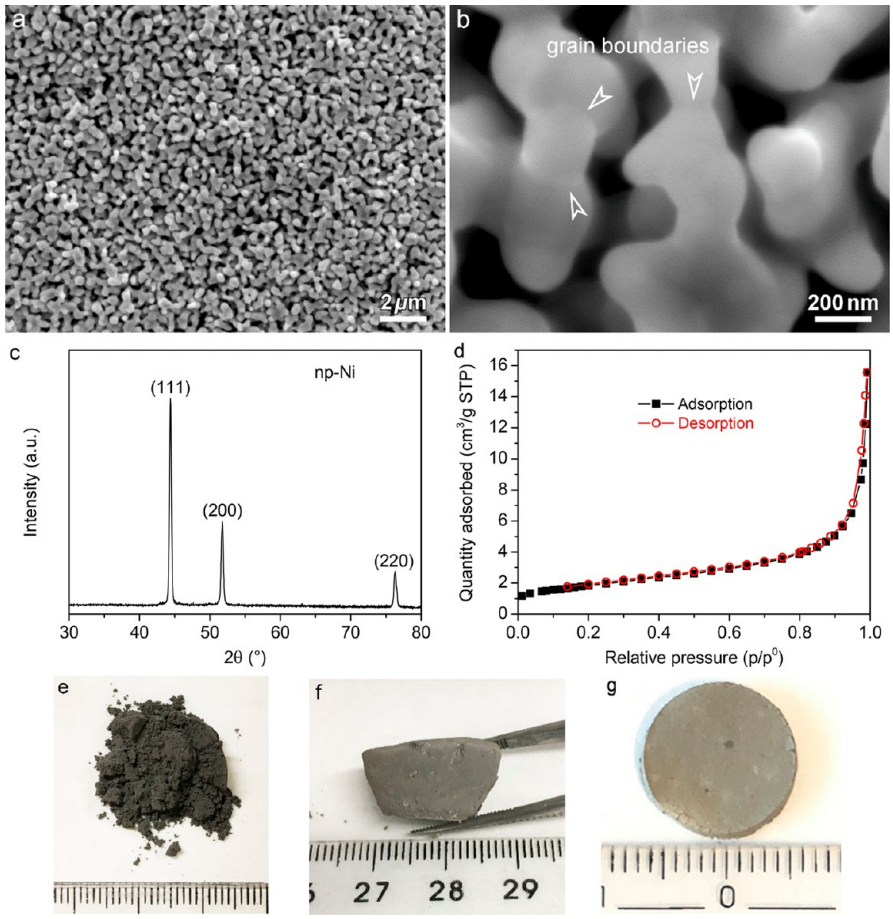

Figure 1. SEM micrographs showing the as-synthesized np-Ni: (a) overview and (b) close view; (c) XRD patterns of np-Ni; (d) the hysteresis curve of N_2 adsorption/desorption isotherm of the hierarchical np-Ni; (e–g) nanoporous metal powders, bulk, and a 13 mm chip.

2.2. Microstructural Characterization. The microstructure of the nanoporous metals was examined with scanning electron microscopy (SEM; Philips FEG-XL30s), X-ray diffraction (XRD; Bruker D8 Advance diffractometer equipped with a Cu Kα source (λ = 0.154 06 nm), and high-resolution transmission electron microscopy (HR-TEM; JEOL JEM-2010F operated at 200 kV). The surface area, porosity, and pore size were detected with N_2 adsorption/desorption experiment at 77 K using a Quantachrome Autosorb-3B surface analyzer.

2.3. Electrochemical Measurements. All of the cells (Swagelok-type cells) were assembled in argon-filled glovebox (MBraun, O_2 < 0.1 ppm and H_2O < 0.1 ppm). Celgard 2500 was used as separator, and Li chips were counter and reference electrodes. The electrolyte was 1 M $LiPF_6$ in a mixture of ethylene carbonate (EC) and diethyl carbonate (DEC) (50:50, v/v). The voltage range for Li ion batteries was controlled within 3.0–0.005 V. The galvanostatic measurements were performed at various current densities from 100 to 2000 mA/g for cyclic performances and rate performances. The cyclic voltammetry (CV) was recorded in the voltage range of 3.0–0.005 V versus Li/Li^+ and at a scanning rate of 0.1 mV/s by μAutolab III-FRA2, EcoChemie. The calculation of the specific capacity was based on the weight of active material $NiC_2O_4{\cdot}2H_2O$. The loading of $NiC_2O_4{\cdot}2H_2O$ equals m{$(C_2O_4{\cdot}2H_2O)^{2-}$} × [molecular weight (MW) of $NiC_2O_4{\cdot}2H_2O$]/[MW of $(C_2O_4{\cdot}2H_2O)^{2-}$] = m{$(C_2O_4{\cdot}2H_2O)^{2-}$} × 1.47, where m{$(C_2O_4{\cdot}2H_2O)^{2-}$} was calculated by subtraction of np-Ni from $NiC_2O_4{\cdot}2H_2O$@np-Ni.

3. RESULTS AND DISCUSSION

3.1. Microstructure of Nanoporous Ni. The as-reported method for producing nanoporous metals and alloys is very facile, because it does not require the addition of any organic compounds or surfactants, neither templates nor solvents. The resources needed are only hydrogen as a reducing agent and metallic salts for providing the metal. The method is based on hydrogen thermal reduction of metallic salts and diffusion-driven growth of metal to form a porous structure. To the best of our knowledge, no work has reported on the synthesis of 3D metallic nanoporous structure by means of a direct hydrogen thermal reduction of metallic salts without any need of templates and complexes.[1,4,6,13,18,26–28]

Figure 1 shows the typical microstructure of as-prepared nanoporous Ni by thermal decomposition and reduction of nickel nitrate hexahydrates at 300 °C for 2 h. The low magnification overview in Figure 1a illustrates that the nanoporous structure is rather uniform. Figure 1b clearly demonstrates a bicontinuous topological nanoporous configuration consisting of interpenetrating nanopores and ligaments. The size of the pores ranged between 25 and 600 nm. The thickness of the ligaments is 100–200 nm. The joints that connected the ligaments are 600–800 nm in size. The grain boundaries observed (marked by the white arrows) in the ligaments and joints imply that the architecture is constructed by Ni grains. Figure 1c shows the XRD pattern of the as-synthesized nanoporous Ni. All of the diffraction peaks are corresponding to pure Ni (standard card JCPDS 04-0850). The ratio of the peak intensity (I) at {111} orientation (abbreviated as $I_{(111)}$) to the peak intensity at {200} orientation ($I_{(200)}$) can judge the preferential growth orientation of Ni grains/ligaments. The ratio $I_{(111)}/I_{(200)}$ is ~2.68, higher than the

DOI: 10.1021/acsanm.8b00284
ACS Appl. Nano Mater. 2018, 1, 2206–2218

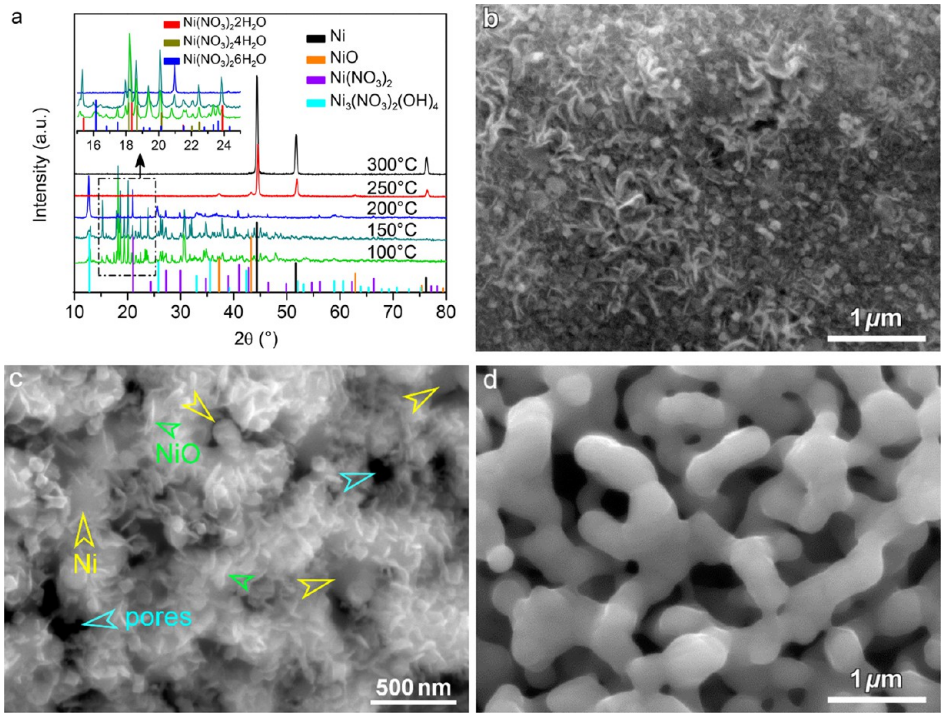

Figure 2. (a) XRD patterns of intermediates formed at different temperatures from 100 to 300 °C revealing the conversion of nickel nitrate hexahydrate to nanoporous Ni at different temperatures in H_2/Ar. (inset) The diffraction peaks within 15−25° 2θ range of the intermediate nickel nitrate hydrates; SEM micrographs showing (b) the microstructure of the intermediates formed at 200 °C, (c) nanoporous product of NiO/Ni mixture formed at 250 °C, and (d) nanoporous Ni formed at 300 °C for 2 h.

normal value of 2.38 referring to the standard XRD card, indicating that the main growth orientation is Ni{111}. Figure 1d shows the N_2 adsorption/desorption isotherm of the hierarchical nanoporous Ni. The specific surface area was measured ~6.58 m^2/g by the Brunauer−Emmett−Teller (BET) method, higher than previous works.[29,30] Notice that some pretreatments of metallic salts such as preheating, premechanical pressing, predissolving, and so forth are applicable before thermal reduction. By controlling the temperature and pretreatment, we successfully synthesized powders, bulk, sheets, and chips as shown in Figure 1e−g. This flexible method makes it feasible for more complex manufacturing processes.

3.2. Reduction Process and Formation Mechanism of Nanoporous Ni. From a metallic salt to a corresponding nanoporous metal, the nonmetal anions are removed, and metal cations become neutralized in the solid phase of a porous structure. For instance, by thermal reduction, nitrate anions and water molecules are eliminated, while Ni^{2+} ions become Ni^0 atoms, which then grow into nanoporous Ni. An overall thermal decomposition and reduction can be summarized as the following reaction:[31]

$$Ni(NO_3)_2\cdot 6H_2O(s) + H_2(g) = Ni(s) + 7H_2O(g) + N_2O_5(g)$$

To understand the transformation process from nickel nitrate hexahydrates to a topological nanoporous Ni framework, we scrutinized the intermediate products by means of XRD. Figure 2a shows the XRD patterns of the products formed at different temperatures from 100 to 300 °C. Below 200 °C, a series of diffraction peaks in the 2θ range of 15−20° (as shown in the inset of Figure 2a) correspond to the nickel nitrate hydrates including hexahydrate, tetrahydrate, and bihydrate, indicating that nickel nitrate hexahydrates melted and then converted to tetrahydrates and bihydrates due to the elimination of water molecules with elevation of the temperature. These intermediates are stable at both 100 and 150 °C. At 200 °C, nickel nitrate anhydrates and $Ni_3(NO_3)_2(OH)_4$ are formed.[31] The layered $Ni_3(NO_3)_2(OH)_4$ and $Ni(NO_3)_2$ further decomposed into NiO with increasing temperature to 250 °C. It demonstrates that, below 250 °C, the thermal decomposition of nickel nitrate hexahydrate dominates. But at 250 °C, the reduction already started, since the strong diffraction peaks of Ni were observed. When the temperature reached 300 °C, the product became fully np-Ni. The partial reduction of NiO implies that the reduction process is a heterogeneous gas−solid reaction. Thus, a transformation of $Ni(NO_3)_2\cdot 6H_2O$ occurred during the heating from room temperature to 300 °C, mainly involving the decomposition of the salt below 250 °C and hydrogen reduction process at or above 250 °C.

The microstructural evolution was inspected by SEM and TEM. Below 200 °C (100 and 150 °C), the intermediates of nickel nitrate hydrates partially comprise rodlike structures (as shown in Figure S1 of the Supporting Information). When the temperature is elevated to 200 °C, nickel nitrate hydrates turn into layered $Ni_3(NO_3)_2(OH)_4$ nanosheets (see Figure 2b) and nickel nitrate.[32] At 250 °C for 2 h, the $Ni_3(NO_3)_2(OH)_4$ nanosheets and nickel nitrate transformed to NiO nanoplates (see Figure 2c marked by a green arrow). At the same time, Ni ligaments (see Figure 2c marked by a yellow arrow) formed internally and were covered by NiO nanoplates. Pores also formed as marked by cyan arrows. It is known that the reduction of NiO has the following process: (i) dissociation of hydrogen atoms at the NiO surface in the induction, diffusion of the hydrogen atoms, and electrons transport, afterward with

DOI: 10.1021/acsanm.8b00284
ACS Appl. Nano Mater. 2018, 1, 2206−2218

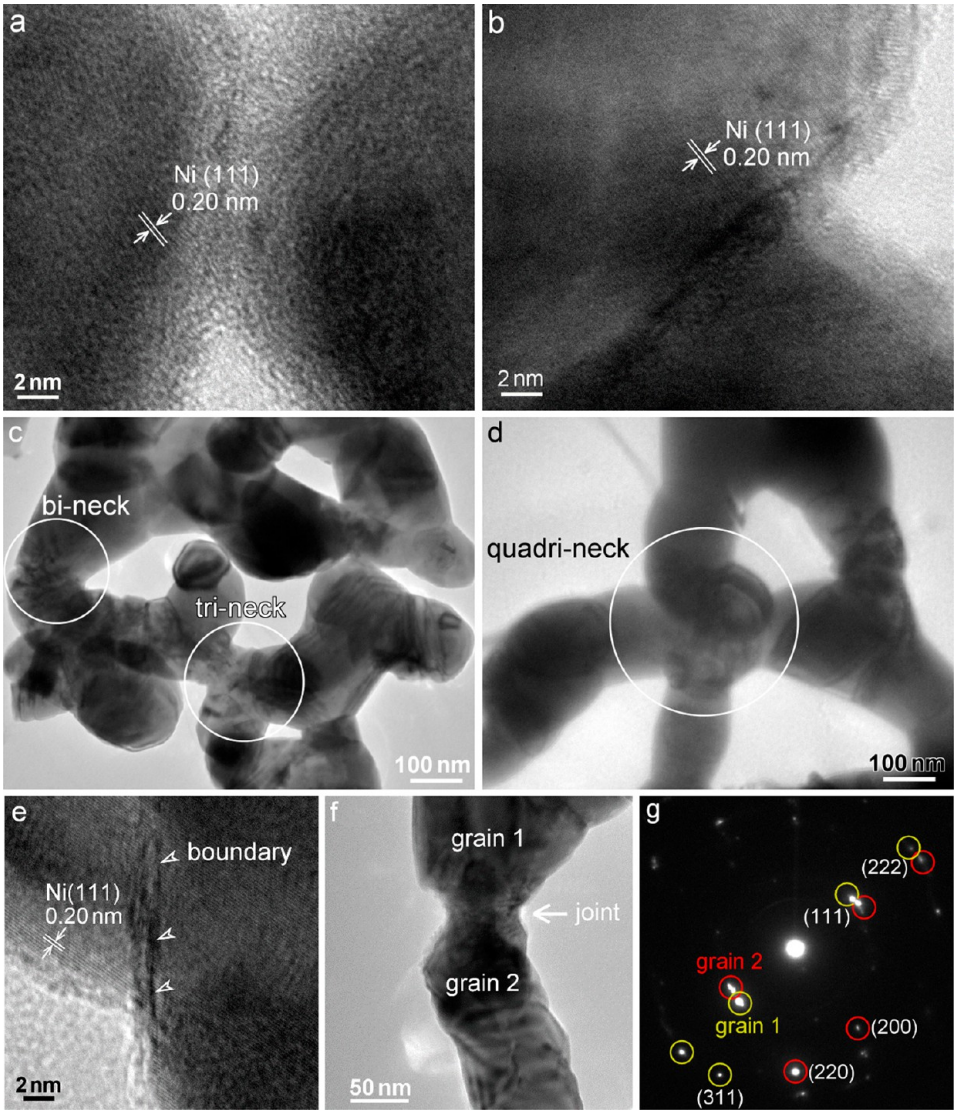

Figure 3. HR-TEM images of (a) the interface at (111) facet of two Ni grains, which are going to form sintering neck at the initial stage and (b) the sintered part of two Ni grains; microstructure of nanoporous Ni: (c) TEM image of bi- and trineck joints, (d) TEM image of a quadri-neck joint, (e) HR-TEM images of the grain boundary of a joint, (f) TEM image of a joint with two ligaments, and (g) the corresponding SAED with the yellow circled dots being for grain 1 (ligament 1) and the red circled dots for grain 2 (ligament 2).

the Ni−O bonds broken and producing metallic Ni atoms; (ii) Ni atoms aggregate to Ni clusters, which accelerate the reduction; (iii) clusters nucleate and form Ni crystallites; finally, the process settles to a pseudo-first-order reaction with respect to nickel.[33,34] It is considered that the formation of Ni ligaments follows with the above processes. Interestingly, we found that if the salt was heated at 300 °C for 1 h, a porous Ni loaded with Ni nanoparticles was obtained (as shown in the Supporting Information Figure S2), indicating that the ligaments were still growing by taking up surrounding Ni nanoparticles. After it was heated for 2 h at 300 °C, a nanoporous Ni formed (see Figure 2d). Thus, the phases and structure encountered rather complex transformations from nickel nitrate hexahydrate to nanoporous Ni.

Regarding the ligament growth from Ni nanocrystallites, TEM was performed to check the particle coalescence in a specimen prepared at 300 °C for 1 h. Figure 3a shows that two Ni particles tend to merge at the interface of {111} facets. Normally, the face-centered cubic (FCC) crystals possess a sequence of surface energies, $\gamma(111) < \gamma(100) < \gamma(110)$.[35] According to the principle of minimum surface free energy, Ni nanoparticles tend to be enclosed by crystallographic facets that have lower energy (in vacuum and strain free), that is, {111} facets. The ligaments form based on this principle, in the form of the coalescence of Ni nanoparticles by the surface diffusion of Ni atoms and grain-boundary migration as shown in Figure 3b. Accordingly, the pores form as a result of vacancies formed during reduction and the ligament growth, which is preferred along {111} facets and by means of coalescence of Ni nanoparticles.

Figure 3c,d shows the microstructure of nanoporous Ni reduced at 300 °C for 2 h. Ni ligaments join each other and form a 3D network. Three types of joints are observed: bineck, trineck, and quadrineck joints. Trineck joints are in the majority, and quadrineck joints are just a few. The joints of nanoporous Ni are constructed by nickel ligaments, which may have different misorientations. To better understand the formation of these joints, we examined the sintering interfaces of the joints as seen in Figure 3e,f. It was confirmed that most of the Ni ligaments sintered at {111} interface to form joints

DOI: 10.1021/acsanm.8b00284
ACS Appl. Nano Mater. 2018, 1, 2206−2218

(Figure 3e). In few joints there were two nickel ligaments, which have different growth orientations sintered together along {111} as shown in Figure 3f. The selected area electron diffraction (SAED) pattern in Figure 3g reveals that the ligament 1 grown along {111} and the ligament 2 grown along {200} sintered together but with a rotation angle of 4.5°.

The mechanisms of the formation of nanoporous metals and growth are schematically illustrated in Figure 4. In this process,

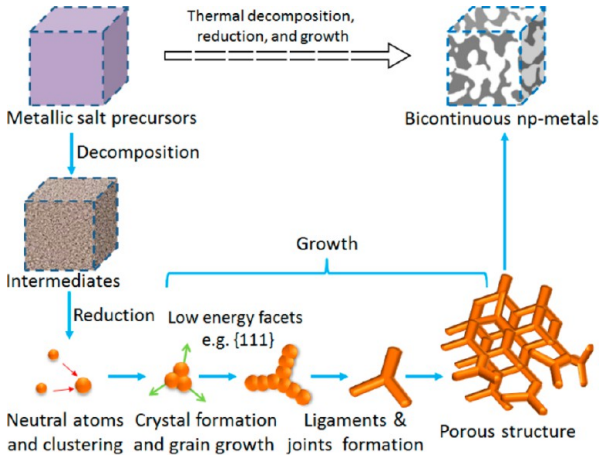

Figure 4. Schematic illustration of the formation process of nanoporous metals from salts by the method of thermal decomposition, reduction, and growth.

a salt thermodynamically decomposes at elevated temperatures, followed with the reduction of its intermediates. By hydrogen reduction, oxygen and/or other nonmetal molecules are removed, which generates vacancies; meanwhile, metal cations become neutral atoms. The formed metal atoms aggregate to clusters, which then nucleate to form Ni nanoparticles. In following, the Ni particles coalesce with other particles mostly on the low surface energy direction {111} interface to form a long ligament. Joints form due to the coalesce of ligaments. Pores form from vacancies formation during reduction and evolve when the joints connect the ligaments. The final porous structure is then constructed by the ligaments, joints, and pores.

3.3. Growth Kinetics of Nanoporous Ni. As Ni grains are building blocks of ligament, the growth of the Ni grains reflects the ligament growth, as well as the porous structure. Thermal growth of grains is primarily influenced by the heating time and temperature. Figure 5 shows the change of the mean grain size of nanoporous Ni with varying heating duration at 300 °C. It was found that with increasing the heating time from 2 to 10 h, the mean grain size increases accordingly from 162 to 348 nm. The ligaments and joints also become larger especially when comparing the samples prepared in 2 and 10 h, respectively. The grain growth is a result of grain-boundary migration by atomic diffusion driven by capillary forces.[36] Under isothermal condition the grain size D varies with time t according to the following equation:

$$D^n - D_0^n = Bt \quad (1)$$

where D_0 is the initial grain size at $t = 0$, which is material related and also affected by the heating rate. B and n are time-independent constants. Normally n is equal to or greater than 2. The D_0 can be taken at the early stage during reduction. We found that, by thermal reduction for 1 h at 300 °C, the product contains many nanoparticles. The size of individual nanoparticles formed at this time can be taken as D_0, which is ~40 nm from the TEM measurement (Supporting Information Figure S2). The constant B follows the Arrhenius equation:

$$B = A \exp(-Q/RT) \quad (2)$$

where A is a constant related to the mobility of Ni atoms, Q is the activation energy of grain growth, R is the ideal gas constant, and T is absolute temperature. On the basis of $t = 2$ h and $D = 162$ nm, we obtain $B = 12\,322$ nm^2/h. At isothermal condition at 300 °C, eq 1 becomes

$$D(nm) = \sqrt{1600 + 12\,322t} \quad (3)$$

Equation 3 depicts the measured grain size very well, as seen in Figure 5d.

The growth orientation of Ni grains by varying the growth time was also studied. Figure 5e shows the XRD patterns of various nanoporous Ni prepared at different growth time from 2 to 10 h at 300 °C. The dominant diffraction peak at ~44.5° corresponds to Ni (111) plane. Figure 5f shows the change of peak intensity ratio $I_{(111)}/I_{(200)}$ with the time variation. It is found that all the $I_{(111)}/I_{(200)}$ ratios are greater than the standard value of 2.38. With increasing the growth time, the ratio of $I_{(111)}/I_{(200)}$ becomes ever larger, revealing that the preferential growth of Ni grains along {111} is time-dependent.

Figures 6 and S3a show the microstructures of nanoporous Ni synthesized at different temperatures from 270 to 800 °C. All samples exhibit a similar topological nanoporous network. It is found that at 270 °C, which is close to the lowest reduction temperature, the nanoporous Ni has the finest ligament size distribution from 50 to 190 nm, with a mean value of ~130 nm. The mean pore size is ~138 nm. At 300 °C, the mean size of ligaments and pores increase slightly to 168 and 180 nm, respectively. When the temperature goes up to 450 °C, the ligaments and pores become larger to 341 and 464 nm, respectively. Apparently, the pore size increases faster than the size of ligaments. This becomes more obvious when the temperature is raised to 600 °C. The ligament size ranges from 472 to 950 nm, with an average of 708 nm. The pores further enlarge in a range from 420 to 1850 nm. At 800 °C, the mean size of ligaments is 1339 nm, and the mean size of pores slightly increases to 1200 nm. Figure 6e clearly shows the dependence of mean size of grains, ligaments, and pores on the temperature. Besides changes in the ligament and pore size with increasing temperature, also the joints increase due to the coalescence of Ni nanoparticles. Kinetically, with rises in the anneal temperature, B exponentially changes according to eq 2, leading to a fast increase of D in the high-temperature region (e.g., between 450 and 800 °C).

Figure 6f shows the evolution of $I_{(111)}/I_{(200)}$ and $I_{(111)}/I_{(200)}$ with increasing growth temperature, determined according to the XRD patterns shown in Figure S3b of nanoporous Ni prepared at different temperatures from 270 to 800 °C. The standard value of $I_{(111)}/I_{(200)}$ is 4.76. Interestingly, with rising temperature, the ratio of $I_{(111)}/I_{(200)}$ becomes smaller from 7.83 at 270° to 4.35 at 800 °C. Meanwhile the $I_{(111)}/I_{(200)}$ ratio decreases from 3.0 to 2.33. It reflects that the temperature can significantly influence the growth orientation. It is inferred that the joints and ligaments coarsened at high temperatures mainly due to the coalescence of grains (as shown in Figures 6d and S3b) along {220} and {200}. Particularly at 800 °C, both {220} and {200} become the dominant growth direction. In contrast, at low temperatures, the formation of thin and long ligaments is mainly based on the grain growth along {111}. Thus, for

DOI: 10.1021/acsanm.8b00284
ACS Appl. Nano Mater. 2018, 1, 2206−2218

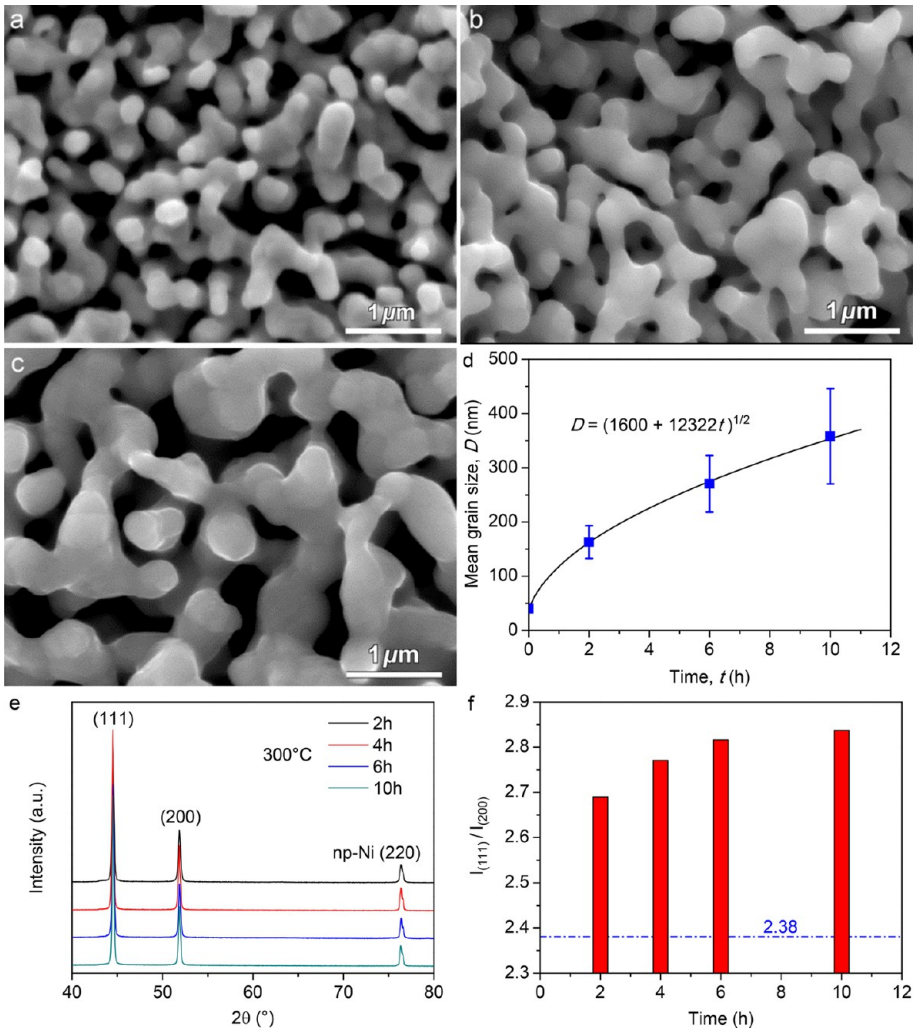

Figure 5. SEM images of nanoporous Ni prepared at 300 °C for different times: (a) 2, (b) 6, and (c) 10 h; (d) the dependence of mean grain size on the heating time; (e) XRD patterns of nanoporous Ni prepared for different growth time at 300 °C; (f) evolution of the peak intensity ratio $I_{(111)}/I_{(200)}$ with the exposure time at 300 °C.

achieving a nanoporous Ni with uniform, thin ligaments and small joints, synthesis at low temperatures is appropriate.

In addition, it is observed that the flow rate of H_2 has no clear influence on the size of pores, grains, and ligaments during the ligament growth (see Supporting Information Figure S4).

3.4. Versatility of the Synthesis Method. The as-reported method was also applied for the synthesis of other nanoporous metals. For example, nanoporous Co was successfully prepared by using cobalt nitrate hexahydrate as a precursor as shown in Figure 7a. The nanoporous Co exhibits a slightly smaller ligament size but similar topological porous structure with np-Ni. Not only pure element nanoporous metals but also nanoporous alloys can be readily prepared. Nanoporous NiCo alloy ($NiCo_2$) was produced with the same approach from the mixture of the nickel nitrate and cobalt nitrate (as shown in Figure 7b). Note that the NiCo alloy has a mesoporous characteristic with an average pore width of ~15 nm. Figure 7c–f shows the uniform distribution of elements of Co and Ni in the nanoporous alloy. Figure 7g presents the XRD patterns of as-synthesized np-Co and np-NiCo alloy. For the alloy, the broader diffraction peaks reveal the smaller grain sizes. This could be due to the growth of grains being hindered by the solid solution.[37] The diffraction peaks of the np-NiCo alloy overlay with that of np-Co but are shifted from that of np-Ni, which is attributed to the partial substitution of Co by Ni atoms. The good uniformity in energy-dispersive X-ray spectroscopy (EDS) and XRD characteristic indicate that the nanoporous alloy comprises atomic substitution of Ni in Co. The above results prove the versatility and convenience of the reported method for the synthesis of different types of nanoporous metals and alloys. The method is superior to the dealloying method for producing nanoporous alloys because of no need of ternary or multielement alloys precursors and special etchants. In addition other salts such as chlorides, acetates, oxalates, hydroxides, and oxides can be used as precursors for synthesizing nanoporous Ni as well (as shown in the Supporting Information Figure S5). It has been proved that all these salts are suitable as precursors for producing nanoporous Ni. This confirms the flexibility and versatility of the reported method for synthesizing nanoporous metals.

3.5. Application of Nanoporous Ni as Current Collectors for Lithium Ion Batteries. Porous metallic structures have promising applications as electrodes for batteries, supercapacitors, fuel cells, electrocatalysts, and hydrogen reduction due to the endowed good mechanical property, rich paths (pores) for ionic diffusion, excellent

DOI: 10.1021/acsanm.8b00284
ACS Appl. Nano Mater. 2018, 1, 2206–2218

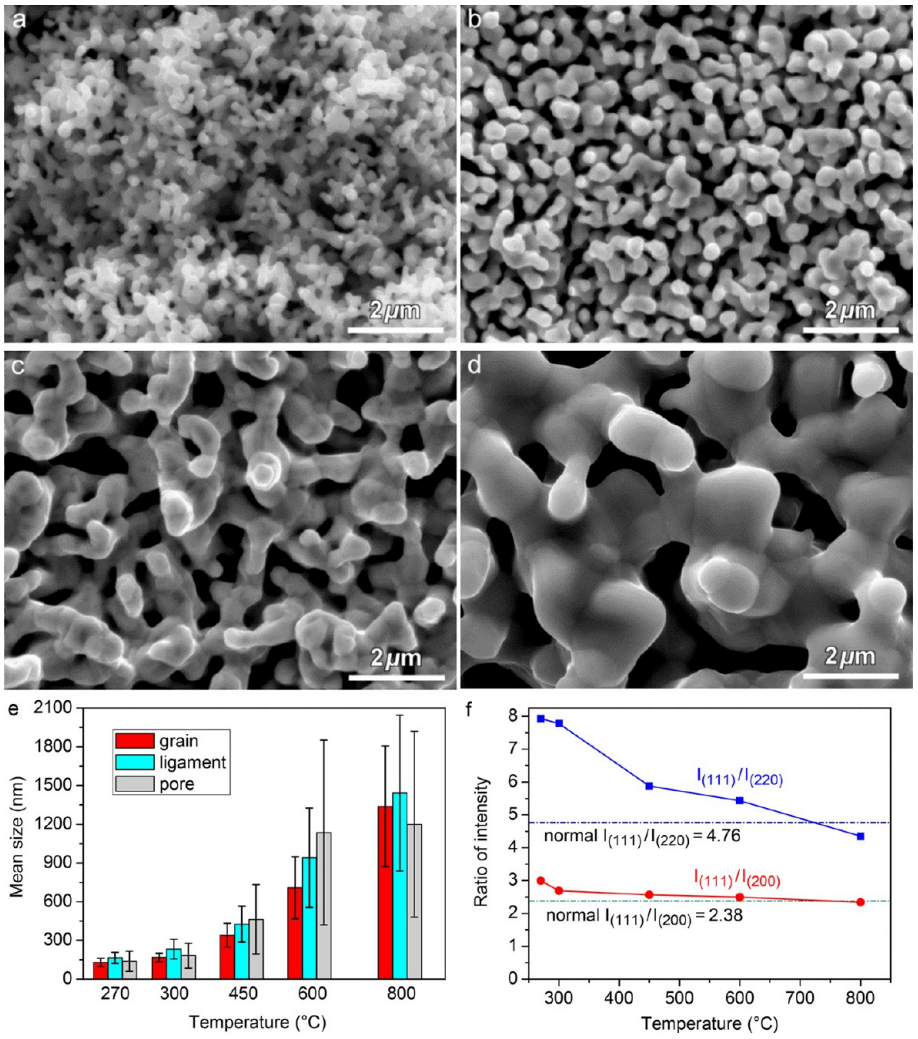

Figure 6. SEM images of nanoporous Ni prepared at different temperatures: (a) 270, (b) 300, (c) 450, and (d) 600 °C; (e) the dependence of mean size of ligament and pores on the heating temperature, and (f) the change of the peak intensity ratios $I_{(111)}/I_{(200)}$ and $I_{(111)}/I_{(220)}$ with varying temperature.

electron transport, and catalysis. In this work, we studied the resistivity and conductivity of nanoporous Ni prepared at different temperatures from 300 to 800 °C by four-point-probe test of Van der Pauw method. As illustrated in Figure 8, with increasing the processing temperature from 300 to 600 °C, the resistivity of np-Ni rapidly decreases from 7.1 to 1.3 $\mu\Omega$·m; meanwhile, its conductivity has an approximately linear increase with rising processing temperature. With increasing processing temperature from 600 to 800 °C, the resistivity and conductivity have slightly changed. A minimum resistivity of 1.2 $\mu\Omega$·m measured for np-Ni synthesized at 800 °C is still much larger than that of bulk Ni (6.99×10^{-2} $\mu\Omega$·m, at 25 °C). The high resistivity of nanoporous Ni synthesized at low processing temperature, for example, 300 °C is attributed to the vast number of defects (e.g., grain boundaries), where the scattering of conduction may contribute to a decrease in electrical conductivity. Annealing at higher temperature can eliminate these defects; thus, the resistivity decreased by raising the temperature to 800 °C.

Because of the good conductivity and porous structure, the nanoporous Ni can be used as bifunctional binder-free current collector and also host for electrodes. Although nickel is heavy and bulk, the porous architecture makes it lighter. The pores can be used for hosting active materials. Thus, the porous architecture can increase the gravimetric and volumetric energy density of electrodes compared with nonporous ones. For example, our synthesized nanoporous Ni has a density ~5.0 g/cm^3 that is much lower than the density of Cu foil current collectors (8.96 g/cm^3). Importantly, the active materials can have intimate contact with metal framework without using conductive additives such as carbon black and binders such as poly(vinylidene fluoride) (PVDF). It also should be mentioned that other nanoporous metal current collectors such as copper can be also synthesized by our method. In this work, we used nanoporous Ni as an example to show the enhanced electrochemical performances by using nanoporous metal current collectors. We synthesized $NiC_2O_4{\cdot}2H_2O$ coated nanoporous Ni as anode of lithium ion batteries as shown in Scheme 1 (step b). Nickel oxalate is a good candidate as anode materials because of their high capacities and abundance. However, the poor electronic conductivity of nickel oxalate and volume expansion during discharge cause fast capacity decay and short service life of the electrodes. To solve the above-mentioned problems, we designed and prepared nanoporous Ni electrodes in which thin $NiC_2O_4{\cdot}2H_2O$ nanofilm coated the Ni ligaments. A facile in situ deposition of $NiC_2O_4{\cdot}2H_2O$

DOI: 10.1021/acsanm.8b00284
ACS Appl. Nano Mater. 2018, 1, 2206−2218

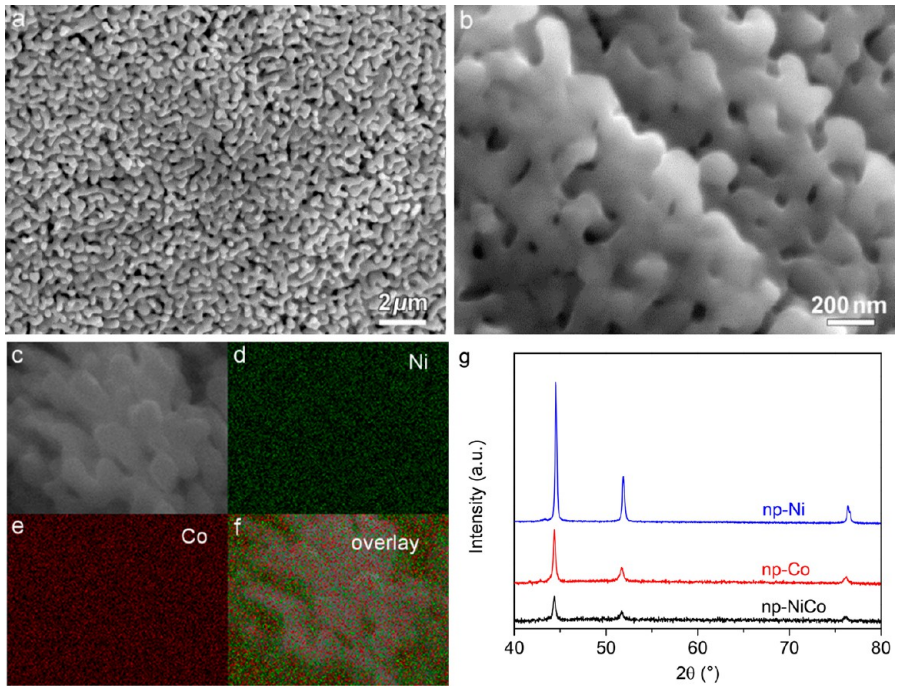

Figure 7. SEM images of (a) nanoporous Co; (b) nanoporous NiCo ($NiCo_2$) alloy; (c–f) SEM image, EDS elements mapping and overlay of nanoporous NiCo; (g) XRD patterns of np-Co and np-NiCo alloy.

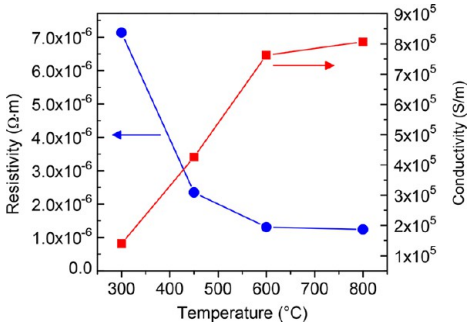

Figure 8. Resistivity and conductivity of nanoporous Ni prepared at different temperatures from 300 to 800 °C.

nanofilms onto Ni ligaments was conducted based on the chemistry between Ni ligaments and oxalic acid, without introducing exotic Ni.[38] Figure 9a shows the microstructures of np-Ni electrodes prepared at 600 °C before being coated with $NiC_2O_4{\cdot}2H_2O$. Figure 9b shows the cross-sectional microstructure of the np-Ni chip coated with $NiC_2O_4{\cdot}2H_2O$ in the nanopores. It displays uniform $NiC_2O_4{\cdot}2H_2O$ nanofilm with a thickness of ~30 nm coated on the ligaments (Figure 9c). Almost no obvious thicker film deposited on the external surface of the np-Ni chip (as seen in Supporting Information Figure S6). XRD pattern of $NiC_2O_4{\cdot}2H_2O$@np-Ni confirmed the formation of nickel oxalate dihydrate coating on np-Ni, and no diffraction peaks of NiO were found as shown in Figure 9d.

Electrochemical measurements were performed to evaluate the electrochemical performances of $NiC_2O_4{\cdot}2H_2O$@np-Ni electrodes. The cyclic voltammetry of $NiC_2O_4{\cdot}2H_2O$@np-Ni electrode (see Figure 10a) shows two cathodic peaks at 1.5 and 0.5 V and three anodic peaks at 1.1, 1.5, 2.3 V, respectively, in the first cycle. From the second cycle, three cathodic peaks positioned at ~1.5, 0.8, and 0.6 V reflect multistep reactions. The large overlaps in the subsequent cycles indicate good electrochemical stability. Galvanostatic charges and discharges were performed within a voltage cutoff window of 3.0–0.005 V. Figure 10b depicts the cyclic performances of $NiC_2O_4{\cdot}2H_2O$@np-Ni electrodes (with ~1.2 mg/cm^2 $NiC_2O_4{\cdot}2H_2O$) against Ni commercial foam (Ni-CF) electrode with loading of $NiC_2O_4{\cdot}2H_2O$ ($NiC_2O_4{\cdot}2H_2O$@Ni-CF, with ~0.28 mg/cm^2 $NiC_2O_4{\cdot}2H_2O$) at the current density of 100 mA/g. Amazingly, the $NiC_2O_4{\cdot}2H_2O$@np-Ni exhibits a superb high specific capacity up to 3154 and 1910 mAh/g for the first discharge and charge, respectively, both of which are much higher than the reported values using oxalates anodes and the nanoporous metal-based SnO_2/nanoporous Cu, MnO_2/nanoporous Cu systems (see Tables S1 and S2 in the Supporting Information).,[39−44] The capacity loss in the first cycle is due to the formation of solid electrolyte interphase (SEI). After 30 cycles, the capacity still remains at 1247 and 1166 mAh/g for the discharge and charge, respectively. The Coulombic efficiency increased from 60.5% of the first cycle to 93.5% of the 30th cycle. In contrast, the $NiC_2O_4{\cdot}2H_2O$@Ni-CF electrode only has capacities of 2223 and 1262 mAh/g for the initial discharge and charge, and it remains at 333 and 257 mAh/g after 30 cycles, respectively. The Coulombic efficiency of $NiC_2O_4{\cdot}2H_2O$@Ni-CF electrode exhibits 56.8% for the first cycle and only 70–80% for the rest cycles. It demonstrates that, by using nanoporous Ni current collectors, all the specific capacity, Coulombic efficiency, and cyclic stability are increased. The improvements of cyclic performances and capacities of $NiC_2O_4{\cdot}2H_2O$@np-Ni electrodes compared with $NiC_2O_4{\cdot}2H_2O$@Ni-CF electrodes are attributed to the higher surface area, smaller pores, and ligaments of np-Ni than commercial macro-Ni foam. So $NiC_2O_4{\cdot}2H_2O$@np-Ni electrodes have thinner $NiC_2O_4{\cdot}2H_2O$ film than in $NiC_2O_4{\cdot}2H_2O$@Ni-CF electrodes when they have similar loading of active materials. As a result, the utilization of $NiC_2O_4{\cdot}2H_2O$ in $NiC_2O_4{\cdot}2H_2O$@np-Ni electrodes could be higher than that in $NiC_2O_4{\cdot}2H_2O$@Ni-CF. Thus, the initial capacity of the $NiC_2O_4{\cdot}2H_2O$@np-Ni

DOI: 10.1021/acsanm.8b00284
ACS Appl. Nano Mater. 2018, 1, 2206–2218

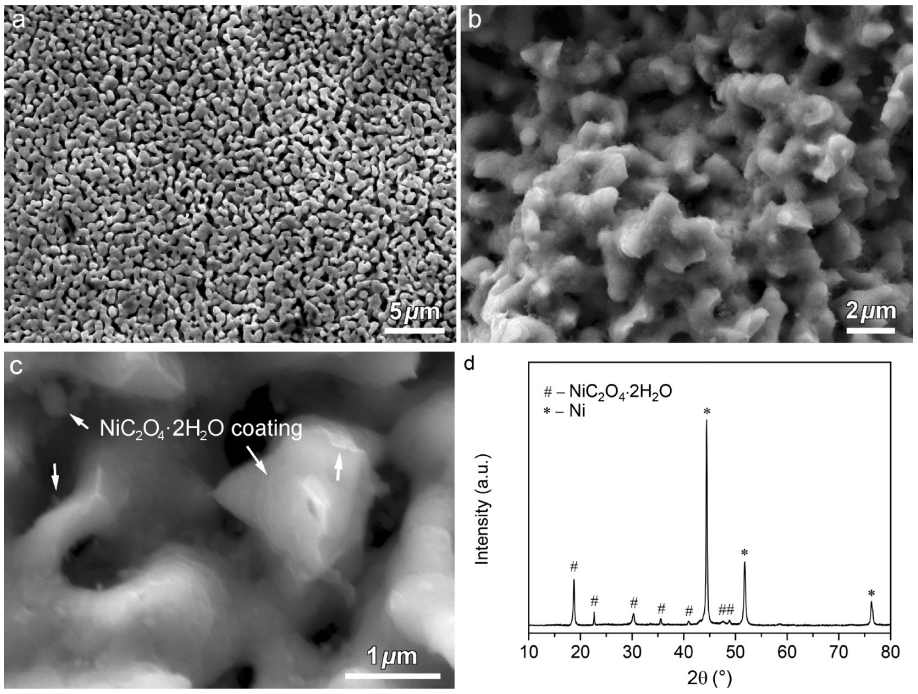

Figure 9. (a) SEM images of microstructure of np-Ni prepared at 600 °C by using $Ni(OH)_2$, (b, c) cross section of $NiC_2O_4{\cdot}2H_2O$@np-Ni chips, and (d) XRD pattern of $NiC_2O_4{\cdot}2H_2O$@np-Ni.

electrode is higher. For the cyclic stability, during discharge and charge the volume expansion of thinner $NiC_2O_4{\cdot}2H_2O$ coatings of $NiC_2O_4{\cdot}2H_2O$@np-Ni electrodes is less than that of $NiC_2O_4{\cdot}2H_2O$@Ni-CF electrodes; thus, the $NiC_2O_4{\cdot}2H_2O$@np-Ni electrodes are more stable than $NiC_2O_4{\cdot}2H_2O$@Ni-CF electrodes. After 30 cycles, the $NiC_2O_4{\cdot}2H_2O$@np-Ni electrodes still have higher capacity retention than $NiC_2O_4{\cdot}2H_2O$@Ni-CF electrodes.

Normally the area loading of active materials can influence the electrochemical performances. Figure 10c displays the cyclic performances of $NiC_2O_4{\cdot}2H_2O$@np-Ni electrodes with different areal loading of $NiC_2O_4{\cdot}2H_2O$ at 100 mA/g. As can be seen, with increasing the areal loading of $NiC_2O_4{\cdot}2H_2O$ from 1.2 to 2.0, 3.1, and 10.1 mg/cm^2, the initial discharge capacities decreased from 3154 to 2346, 1480, and 873 mAh/g, respectively. Meanwhile, the charge capacities also dropped from 1910 to 1545, 888 down to 528 mAh/g, respectively. So with raising the loading of active materials, the capacity drops, and the utilization of $NiC_2O_4{\cdot}2H_2O$ becomes lower. After 30 cycles, the reversible capacities of electrodes with areal $NiC_2O_4{\cdot}2H_2O$ loading of 1.2, 2.0, 3.1, and 10.1 mg/cm^2 remained at 1247, 901, 282, and 194 mAh/g, respectively. It presents that fast capacity decay occurs on electrodes with high loading of $NiC_2O_4{\cdot}2H_2O$ (3.0−10.1 mg/cm^2). With increasing the loading of active materials, the lower capacity and faster decays can be explained by the following reasons: (i) the higher loading of $NiC_2O_4{\cdot}2H_2O$ (3.0−10.1 mg/cm^2) means thicker coatings. Their lower capacities indicated lower utilization of $NiC_2O_4{\cdot}2H_2O$, which can be ascribed to the higher transport resistance between Ni ligaments and thicker $NiC_2O_4{\cdot}2H_2O$ coating. In comparison, the thinner $NiC_2O_4{\cdot}2H_2O$ coating (2.0 mg/cm^2 corresponding to ∼30 nm thick film) has higher electric conductivity. Thus, the thinner $NiC_2O_4{\cdot}2H_2O$ coating can be fully utilized. (ii) The electrodes with higher loading of $NiC_2O_4{\cdot}2H_2O$ (3.0−10.0 mg/cm^2) suffered from faster capacity decay could be owing to both the poor electric transport and severe volume expansion. Thicker $NiC_2O_4{\cdot}2H_2O$ coatings have bigger volume expansion, which may cause heavier pulverization. So the SEI may encounter repeated damage and reformation, resulting in thick SEI. To test the size effect of $NiC_2O_4{\cdot}2H_2O$ on battery performances and the advantages of as-synthesized conformal coating, we prepared and measured the performances of $NiC_2O_4{\cdot}2H_2O$ nanowires standing growth on Ni ligaments (as shown in Figure S7a,b). It is found that the $NiC_2O_4{\cdot}2H_2O$ nanowires had very poor initial capacities and very fast capacity decay as shown in Figure S7c, which reflects the fact that the large size of $NiC_2O_4{\cdot}2H_2O$ and poor contacts between $NiC_2O_4{\cdot}2H_2O$ and Ni ligaments are severely harmful to the electrochemical performances due to the poor electric conductivity of $NiC_2O_4{\cdot}2H_2O$.[39]

In addition, we also tested the electrochemical performances of $NiC_2O_4{\cdot}2H_2O$@np-Ni electrode (with a loading below 1.2 mg/cm^2) at higher current density. The batteries first discharged and charged at 100 mA/g for four cycles to achieve full activation, followed with discharge and charge at 500 mA/g. Figure 10d shows the high reversible capacities and good stability; for instance, a high discharge capacity of 1253 mAh/g still remains after 40 cycles. The good performances at high rate could be contributed to the intimate contact between $NiC_2O_4{\cdot}2H_2O$ nanocoating and nanoporous Ni current collectors. The nanoporous Ni current collectors also provide high surface area and porous rooms for active materials, and they enhanced the electric conductivity of electrodes.

The as-developed $NiC_2O_4{\cdot}2H_2O$@np-Ni electrodes significantly improved the gravimetric and volumetric capacity densities as well as the areal capacities. In previous studies a big problem about the application of porous metal current collectors was the low areal and volumetric loading of active materials, which caused the low gravimetric and volumetric energy density calculation based on the overall weight of electrodes.[3,6,24,41,45−53] The use of copper substrates as supports for nanoporous metal current collector films

DOI: 10.1021/acsanm.8b00284
ACS Appl. Nano Mater. 2018, 1, 2206−2218

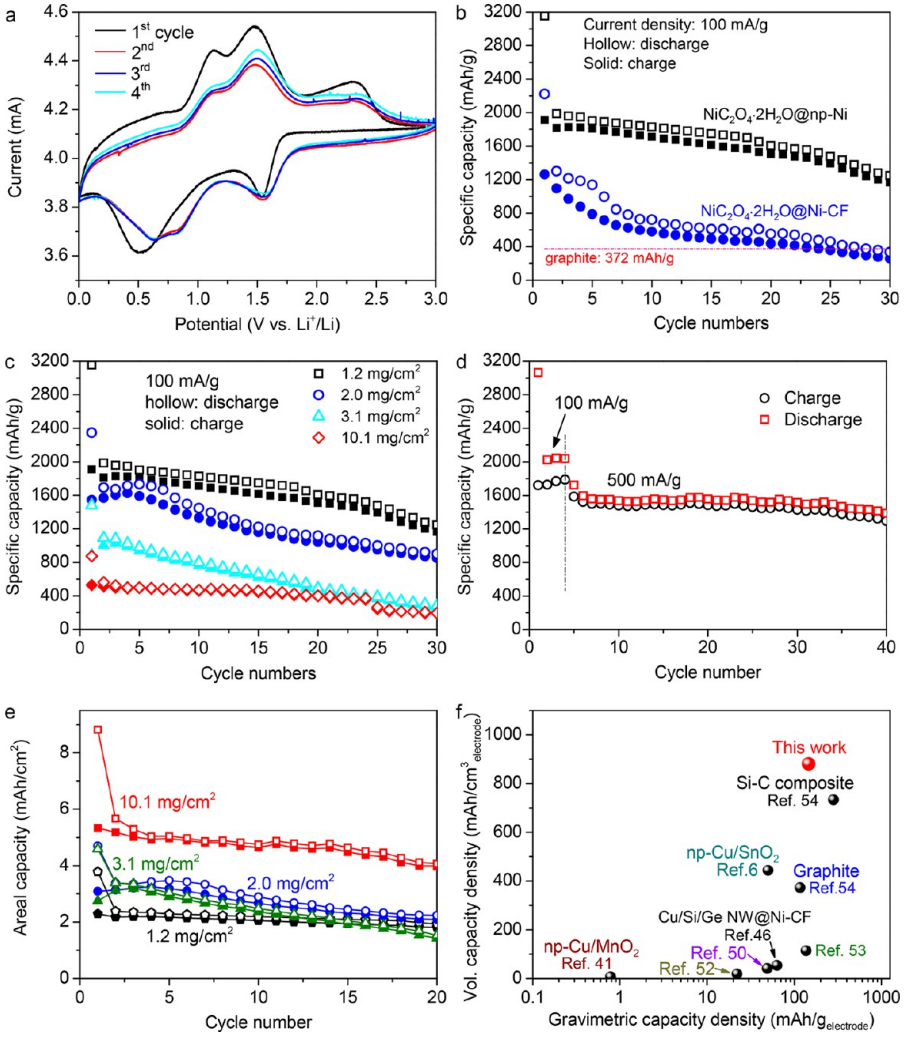

Figure 10. (a) CV curve of $NiC_2O_4{\cdot}2H_2O$@np-Ni with scanning rate at 0.1 mV/s in the potential window of 3.0−0.005 V; (b) the cycling performances of $NiC_2O_4{\cdot}2H_2O$@np-Ni and $NiC_2O_4{\cdot}2H_2O$@Ni-CF at 100 mA/g; (c) the cycling performances of $NiC_2O_4{\cdot}2H_2O$@np-Ni with various loadings of $NiC_2O_4{\cdot}2H_2O$ at 100 mA/g; (d) the cycling performances of $NiC_2O_4{\cdot}2H_2O$@np-Ni at 500 mA/g; (e) the areal capacity densities of $NiC_2O_4{\cdot}2H_2O$@np-Ni with different loading of $NiC_2O_4{\cdot}2H_2O$; (f) comparison of the gravimetric and volumetric capacity densities of $NiC_2O_4{\cdot}2H_2O$@np-Ni electrode developed in this work with other reported electrodes.

significantly decreases the gravimetric and volumetric capacity density of overall electrodes.[6,41] To overcome these problems, we increased the areal loading of active metals and prepared mechanical stale current collectors without using copper substrates. The initial areal capacity density of $NiC_2O_4{\cdot}2H_2O$@np-Ni electrodes approached 8.8 mAh/cm^2, which is also much higher than np-Cu/SnO_2, np-Cu/MnO_2, np-Cu@Cu_2O, Cu/Si/Ge NW@Ni-CF, $NiCo_2O_4$@Ni-CF, Si−C composites, Si/C−graphite electrodes, and graphite anode.[6,41,44−54] It still stabilized at ∼4.0 mAh/cm^2 after 20 cycles (see Figure 10e), which is also a quite high areal capacity. It is found when using the loading of 10.1 mg/cm^2, the capacity density based on electrodes can reach 881 mAh/cm^3 for maximum volumetric and 189 mAh/g for maximum gravimetric, which are much higher than those of previous metallic current collector electrodes such as np-Cu/SnO_2,[6] np-Cu/MnO_2,[41] NP Cu@Cu_2O,[45] Cu/Si/Ge NW@Ni-CF,[46] $ZnCo_2O_4$@Ni-CF,[50] NiO@Ni-CF,[51] $ZnCo_2O_4$−ZnO−C@Ni-CF,[52] Co_3O_4@Co_3S_4@Ni-CF,[53] graphite anodes (1.3 g/cm^3, and calculated with a theoretical capacity of 372 mAh/g) on the Cu foil (18 μm thick for half cells), as well as the volumetric energy density of Si−C electrodes on Cu foil (∼734 mAh/cm^3, see the calculations, Figure 10f and Table S2 in Supporting Information).[54] It should be pointed out that, when using a copper foil with a thickness of ∼10 μm in commercial use, the theoretical gravimetric capacity density and volumetric capacity density of graphite anode will increase to 164 mAh/g and 414 mAh/cm^3. The volumetric capacity density of $NiC_2O_4{\cdot}2H_2O$@np-Ni is still much higher than that of graphite anodes. The gravimetric capacity density of $NiC_2O_4{\cdot}2H_2O$@np-Ni is lower than that of Si−C composites/Cu foil electrodes (∼282 mAh/g),[54] but it can be fully believed that a higher gravimetric and volumetric capacity density of nanoporous metal electrodes can be achieved if increasing the loading of active materials or using active materials with high specific capacities such as Si or Sn in future works. To that end, the electrodes using binder-free nanoporous metal current collectors exhibit ultrahigh gravimetric, volumetric capacity density, and areal capacities, which provides new strategies not only for lithium ion batteries but also for other electric storage devices such as sodium ion batteries, aluminum ion batteries, and supercapacitors.

DOI: 10.1021/acsanm.8b00284
ACS Appl. Nano Mater. 2018, 1, 2206−2218

4. CONCLUSION

In this paper, a facile and novel synthesis of nanoporous metals by the hydrogen thermal reduction and growth of metallic salts was developed. The as-obtained porous Ni comprises topological porous structure with nanopores and ligaments. Different shapes, sizes of bulk, sheets, and powders were produced. The growth kinetics and the formation mechanism were studied. The method can also be applied for the synthesis of other nanoporous metallic alloys systems by using other precursors such as nitrates, chlorides, oxalates, acetates, hydroxides, and oxides. The as-synthesized $NiC_2O_4{\cdot}2H_2O$@np-Ni exhibited a good electrochemical performance. The paper provides a novel, facile, and economic strategy for industrial production of nanoporous metals and the application of nanoporous metals for energy storage.

■ ASSOCIATED CONTENT

Supporting Information

The Supporting Information is available free of charge on the ACS Publications website at DOI: 10.1021/acsanm.8b00284.

Additional figures and information including microstructures of intermediates between temperatures from 100 to 300 °C, microstructures of np-Ni synthesized under different flow rate; microstructures of np-Ni prepared at 800 °C; XRD patterns of nanoporous Ni prepared at different temperature; microstructures of porous Ni synthesized by using different salts; SEM images of the deposition of NiC_2O_4 coating on internal and external of ligaments; morphologies, discharge, and charge profiles of $NiC_2O_4{\cdot}2H_2O$@np-Ni nanowires; calculations on capacity densities of graphite electrodes; tables on comparisons of electrochemical performances with previous works (PDF)

■ AUTHOR INFORMATION

Corresponding Author

*E-mail: y.pei@rug.nl.

ORCID

Yutao Pei: 0000-0002-1817-2228

Notes

The authors declare no competing financial interest.

■ ACKNOWLEDGMENTS

The authors gratefully acknowledge the financial support from the Faculty of Science and Engineering, Univ. of Groningen, The Netherlands.

■ REFERENCES

(1) Kränzlin, N.; Niederberger, M. Controlled Fabrication of Porous Metals from the Nanometer to the Macroscopic Scale. *Mater. Horiz.* **2015**, *2*, 359−377.

(2) Detsi, E.; Onck, P.; De Hosson, J. T. M. Metallic Muscles at Work: High Rate Actuation in Nanoporous Gold/Polyaniline Composites. *ACS Nano* **2013**, *7*, 4299−4306.

(3) Lang, X. Y.; Hirata, A.; Fujita, T.; Chen, M. W. Nanoporous Metal/oxide Hybrid Electrodes for Electrochemical Supercapacitors. *Nat. Nanotechnol.* **2011**, *6*, 232−236.

(4) Banhart, J. Manufacture, Characterisation and Application of Cellular Metals and Metal Foams. *Prog. Mater. Sci.* **2001**, *46*, 559−632.

(5) Qiu, H. J.; Kang, J. L.; Liu, P.; Hirata, A.; Fujita, T.; Chen, M. W. Fabrication of Large-scale Nanoporous Nickel with a Tunable Pore Size for Energy Storage. *J. Power Sources* **2014**, *247*, 896−905.

(6) Hou, C.; Shi, X. M.; Zhao, C. X.; Lang, X. Y.; Zhao, L. L.; Wen, Z.; Zhu, Y. F.; Zhao, M.; Li, J. C.; Jiang, Q. A. SnO_2 Nanoparticles Embedded in 3D Nanoporous/ Solid Copper Current Collectors for High Performance Reversible Lithium Storage. *J. Mater. Chem. A* **2014**, *2*, 15519−15526.

(7) Kas, R.; Hummadi, K. K.; Kortlever, R.; De Wit, P.; Milbrat, A.; Luiten-Olieman, M. W. J.; Benes, N. E.; Koper, M. T. M.; Mul, G. Three-dimensional Porous Hollow Fibre Copper Electrodes for Efficient and High-rate Electrochemical Carbon Dioxide Reduction. *Nat. Commun.* **2016**, *7*, 10748.

(8) Lu, Q.; Hutchings, G. S.; Yu, W. T.; Zhou, Y.; Forest, R. V.; Tao, R. Z.; Rosen, J.; Yonemoto, B. T.; Cao, Z. Y.; Zheng, H. M.; Xiao, J. Q.; Jiao, F.; Chen, J. G. Highly Porous Non-precious Bimetallic Electrocatalysts for Efficient Hydrogen Evolution. *Nat. Commun.* **2015**, *6*, 6567.

(9) Ge, X. B.; Chen, L. Y.; Zhang, L.; Wen, Y. R.; Hirata, A.; Chen, M. W. Nanoporous Metal Enhanced Catalytic Activities of Amorphous Molybdenum Sulfide for High-efficiency Hydrogen Production. *Adv. Mater.* **2014**, *26*, 3100−3104.

(10) Ito, Y.; Tanabe, Y.; Qiu, H. J.; Sugawara, K.; Heguri, S.; Tu, N. H.; Huynh, K. K.; Fujita, T.; Takahashi, T.; Tanigaki, K.; Chen, M. W. High-quality Three-dimensional Nanoporous Graphene. *Angew. Chem.* **2014**, *126*, 4922−4926.

(11) Tian, J.; Lu, T. J.; Hodson, H. P.; Queheillalt, D. T.; Wadley, H. N. G. Cross Flow Heat Exchange of Textile Cellular Metal Core Sandwich Panels. *Int. J. Heat Mass Transfer* **2007**, *50*, 2521−2536.

(12) Zhang, Y.; Luc, W.; Hutchings, G. S.; Jiao, F. Photo-electrochemical Carbon Dioxide Reduction Using a Nanoporous Ag Cathode. *ACS Appl. Mater. Interfaces* **2016**, *8*, 24652−24658.

(13) Tappan, B. C.; Steiner, S. A., III; Luther, E. P. Nanoporous Metal Foams. *Angew. Chem., Int. Ed.* **2010**, *49*, 4544−4565.

(14) Simone, A. E.; Gibson, L. J. The Tensile Strength of Porous Copper Made by the GASAR Process. *Acta Mater.* **1996**, *44*, 1437−1447.

(15) Ryan, G.; Pandit, A.; Apatsidis, D. P. Fabrication Methods of Porous Metals for Use in Orthopaedic Applications. *Biomaterials* **2006**, *27*, 2651−2670.

(16) Yavuz, M. S.; Cheng, Y.; Chen, J.; Cobley, C. M.; Zhang, Q.; Rycenga, M.; Xie, J.; Kim, C.; Song, K. H.; Schwartz, A. G.; Wang, L. V.; Xia, Y. N. Gold Nanocages Covered by Smart Polymers for Controlled Release with Near-infrared Light. *Nat. Mater.* **2009**, *8*, 935−939.

(17) Detsi, E.; Punzhin, S.; Onck, P. R.; De Hosson, J. T. M. Direct Synthesis of Metal Nanoparticles with Tunable Porosity. *J. Mater. Chem.* **2012**, *22*, 4588−4591.

(18) Dumée, L. F.; He, L.; Lin, B.; Ailloux, F. M.; Lemoine, J. B.; Velleman, L.; She, F. H.; Duke, M. C.; Orbell, J. D.; Erskine, G.; Hodgson, P. D.; Gray, S.; Kong, L. X. The Fabrication and Surface Functionalization of Porous Metal Frameworks − A Review. *J. Mater. Chem. A* **2013**, *1*, 15185−15206.

(19) Yu, L. P.; Lei, T.; Nan, B.; Jiang, Y.; He, Y.; Liu, C. T. Characteristics of A Sintered Porous Ni-Cu Alloy Cathode for Hydrogen Production in A Potassium Hydroxide Solution. *Energy* **2016**, *97*, 498−505.

(20) Liang, K.; Li, L.; Yang, Y. Inorganic Porous Films for Renewable Energy Storage. *ACS Energy Lett.* **2017**, *2*, 373−390.

(21) Liang, K.; Marcus, K.; Zhang, S. F.; Zhou, L.; Li, Y. L.; De Oliveira, S. T.; Orlovskaya, N.; Sohn, Y.-H.; Yang, Y. NiS_2/FeS Holey Film as Freestanding Electrode for High-performance Lithium Battery. *Adv. Energy Mater.* **2017**, *7*, 1701309.

(22) Ying, J.; Yang, X. Y.; Tian, G.; Janiak, C.; Su, B. L. Self-assembly: An Option to Nanoporous Metal Nanocrystals. *Nanoscale* **2014**, *6*, 13370−13382.

(23) Kreder, K. J., III; Manthiram, A. Metal Nanofoams via A Facile Microwave-assisted Solvothermal Process. *Chem. Commun.* **2017**, *53*, 865−868.

(24) Guo, X. W.; Han, J. H.; Zhang, L.; Liu, P.; Hirata, A.; Chen, L. Y.; Fujita, T.; Chen, M. W. A Nanoporous Metal Recuperated MnO_2 Anode for Lithium Ion Batteries. *Nanoscale* **2015**, *7*, 15111−15116.

DOI: 10.1021/acsanm.8b00284
ACS Appl. Nano Mater. 2018, 1, 2206−2218

(25) Zhang, H. G.; Yu, X. D.; Braun, P. V. Three-dimensional Bicontinuous Ultrafast-charge and -discharge Bulk Battery Electrodes. *Nat. Nanotechnol.* **2011**, *6*, 277−281.
(26) Luidold, S.; Antrekowitsch, H. Hydrogen as A Reducing Agent: State-of-the-art Science and Technology. *JOM* **2007**, *59*, 20−26.
(27) Sokić, M.; Kamberović, Z.; Nikolić, V.; Marković, B.; Korać, M.; Anđić, Z.; Gavrilovski, M. Kinetics of NiO and $NiCl_2$ Hydrogen Reduction as Precursors and Properties of Produced Ni/Al_2O_3 and $Ni-Pd/Al_2O_3$ Catalysts. *Sci. World J.* **2015**, *2015*, 601970.
(28) Suh, Y. J.; Jang, H. D.; Chang, H.; Kim, W. B.; Kim, H. C. Size-controlled Synthesis of Fe-Ni Alloy Nanoparticles by Hydrogen Reduction of Metal Chlorides. *Powder Technol.* **2006**, *161*, 196−201.
(29) Walsh, D.; Arcelli, L.; Ikoma, T.; Tanaka, J.; Mann, S. Dextran Templating for the Synthesis of Metallic and Metal Oxide Sponges. *Nat. Mater.* **2003**, *2*, 386−390.
(30) Erri, P.; Nader, J.; Varma, A. Controlling Combustion Wave Propagation for Transition Metal/Alloy/Cermet Foam Synthesis. *Adv. Mater.* **2008**, *20*, 1243−1245.
(31) Brockner, W.; Ehrhardt, C.; Gjikaj, M. Thermal Decomposition of Nickel Nitrate Hexahydrate, $Ni(NO_3)_2{\cdot}6H_2O$, in Comparison to $Co(NO_3)_2{\cdot}6H_2O$ and $Ca(NO_3)_2{\cdot}4H_2O$. *Thermochim. Acta* **2007**, *456*, 64−68.
(32) Tong, G. X.; Hu, Q.; Wu, W. H.; Li, W.; Qian, H. S.; Liang, Y. Submicrometer-sized NiO Octahedra: Facile One-pot Solid Synthesis, Formation Mechanism, and Chemical Conversion into Ni Octahedra with Excellent Microwave-absorbing Properties. *J. Mater. Chem.* **2012**, *22*, 17494−17504.
(33) Richardson, J. T.; Scates, R.; Twigg, M. V. X-Ray Diffraction Study of Nickel Oxide Reduction by Hydrogen. *Appl. Catal., A* **2003**, *246*, 137−150.
(34) Jeangros, Q.; Hansen, T. W.; Wagner, J. B.; Damsgaard, C. D.; Dunin-Borkowski, R. E.; Hebert, C.; Van herle, J.; Hessler-Wyser, A. Reduction of Nickel Oxide Particles by Hydrogen Studied in an Environmental TEM. *J. Mater. Sci.* **2013**, *48*, 2893−2907.
(35) Xiong, Y. J.; Wiley, B.; Xia, Y. N. Nanocrystals with Unconventional Shapes − A Class of Promising Catalysts. *Angew. Chem., Int. Ed.* **2007**, *46*, 7157−7159.
(36) Chen, I. W.; Wang, X. H. Sintering Dense Nanocrystalline Ceramics without Final-stage Grain Growth. *Nature* **2000**, *404*, 168−171.
(37) Wu, Z.; Bei, H.; Otto, F.; Pharr, G. M.; George, E. P. Recovery, Recrystallization, Grain Growth and Phase Stability of A Family of FCC-structured Multi-component Equiatomic Solid Solution Alloys. *Intermetallics* **2014**, *46*, 131−140.
(38) Jung, I.; Choi, J.; Tak, Y. Nickel Oxalate Nanostructures for Supercapacitors. *J. Mater. Chem.* **2010**, *20*, 6164−6169.
(39) Oh, H. J.; Jo, C. H.; Yoon, C. S.; Yashiro, H.; Kim, S. J.; Passerini, S.; Sun, Y. K.; Myung, S. T. Nickel Oxalate Dihydrate Nanorods Attached to Reduced Graphene Oxide Sheets as A High-capacity Anode for Rechargeable Lithium Batteries. *NPG Asia Mater.* **2016**, *8*, 270.
(40) Aragón, M. J.; León, B.; Serrano, T.; Perez Vicente, C.; Tirado, J. L. Synergistic Effects of Transition Metal Substitution in Conversion Electrodes for Lithium-ion Batteries. *J. Mater. Chem.* **2011**, *21*, 10102−10107.
(41) Hou, C.; Lang, X. Y.; Han, G. F.; Li, Y. Q.; Zhao, L.; Wen, Z.; Zhu, Y. F.; Zhao, M.; Li, J. C.; Lian, J. S.; Jiang, Q. Integrated Solid/Nanoporous Copper/Oxide Hybrid Bulk Electrodes for High-performance Lithium-ion Batteries. *Sci. Rep.* **2013**, *3*, 2878.
(42) López, M. C.; Tirado, J. L.; Perez Vicente, C. Structural and Comparative Electrochemical Study of M(II) Oxalates, M = Mn, Fe, Co, Ni, Cu, Zn. *J. Power Sources* **2013**, *227*, 65−71.
(43) Xu, J. M.; He, L.; Liu, H.; Han, T.; Wang, Y. J.; Zhang, C. J.; Zhang, Y. H. Controlled Synthesis of Porous Anhydrous Cobalt Oxalate Nanorods with High Reversible Capacity and Excellent Cycling Stability. *Electrochim. Acta* **2015**, *170*, 85−91.
(44) León, B.; Vicente, C. P.; Tirado, J. L. New Mixed Transition Metal Oxysalts as Negative Electrode Materials for Lithium-ion Batteries. *Solid State Ionics* **2012**, *225*, 518−521.
(45) Liu, D. Q.; Yang, Z. B.; Wang, P.; Li, F.; Wang, D. S.; He, D. Y. Preparation of 3D Nanoporous Copper-supported Cuprous oxide for High-performance Lithium Ion Battery Anodes. *Nanoscale* **2013**, *5*, 1917−1921.
(46) Zhang, Q. B.; Chen, H. X.; Luo, L. L.; Zhao, B. T.; Luo, H.; Han, X.; Wang, J. W.; Wang, C. M.; Yang, Y.; Zhu, T.; Liu, M. L. Harnessing the Concurrent Reaction Dynamics in Active Si and Ge to Achieve High Performance Lithium-ion Batteries. *Energy Environ. Sci.* **2018**, *11*, 669.
(47) Li, X. L.; Yan, P. F.; Xiao, X. C.; Woo, J. H.; Wang, C. M.; Liu, J.; Zhang, J. G. Design of Porous Si/C−graphite Electrodes with Long Cycle Stability and Controlled Swelling. *Energy Environ. Sci.* **2017**, *10*, 1427−1434.
(48) Song, H. C.; Wang, H. X.; Lin, Z. X.; Jiang, X. F.; Yu, L. W.; Xu, J.; Yu, Z. W.; Zhang, X. W.; Liu, Y. J.; He, P.; Pan, L. J.; Shi, Y.; Zhou, H. S.; Chen, K. J. Highly Connected Silicon-copper Alloy Mixture Nanotubes as High-rate and Durable Anode Materials for Lithium-ion Batteries. *Adv. Funct. Mater.* **2016**, *26*, 524−531.
(49) Mukanova, A.; Nurpeissova, A.; Urazbayev, A.; Kim, S.-S.; Myronov, M.; Bakenov, Z. Silicon Thin Film on Graphene Coated Nickel Foam as An Anode for Li-ion Batteries. *Electrochim. Acta* **2017**, *258*, 800−806.
(50) Qu, B. H.; Hu, L. L.; Li, Q. H.; Wang, Y. G.; Chen, L. B.; Wang, T. H. High-performance Lithium-ion Battery Anode by Direct Growth of Hierarchical $ZnCo_2O_4$ Nanostructures on Current Collectors. *ACS Appl. Mater. Interfaces* **2014**, *6*, 731−736.
(51) Yang, W. F.; Cheng, G. H.; Dong, C. Q.; Bai, Q. G.; Chen, X. T.; Peng, Z. Q.; Zhang, Z. H. NiO Nanorod Array Anchored Ni Foam as A Binder Free Anode for High-rate Lithium ion Batteries. *J. Mater. Chem. A* **2014**, *2*, 20022−20029.
(52) Li, Z. Q.; Yin, L. W. Sandwich-like Reduced Graphene oxide Wrapped MOF-derived $ZnCo_2O_4$−ZnO−C on Nickel Foam as Anodes for High Performance Lithium Ion Batteries. *J. Mater. Chem. A* **2015**, *3*, 21569−21577s.
(53) Wang, X.; Liu, C. K.; Li, Q.; Li, H. S.; Xu, J.; Chu, X. M.; Zhang, L. J.; Zhao, G. X.; Li, H. L.; Guo, P. Z.; Li, S. D.; Zhao, X. S. 3D Heterogeneous Co_3O_4@Co_3S_4 Nanoarrays Grown on Ni Foam as a Binder-free Electrode for Lithium-ion Batteries. *ChemElectroChem* **2018**, *5*, 309−315.
(54) Magasinski, A.; Dixon, P.; Hertzberg, B.; Kvit, A.; Ayala, J.; Yushin, G. High-performance Lithium-ion Anodes Using a Hierarchical Bottom-up Approach. *Nat. Mater.* **2010**, *9*, 353−358.

NOTE ADDED AFTER ASAP PUBLICATION

This paper was published ASAP on April 26, 2018 with incorrect Supporting Information files. The paper and new Supporting Information files were reposted on May 2, 2018.

DOI: 10.1021/acsanm.8b00284
ACS Appl. Nano Mater. 2018, 1, 2206−2218